Inverse Problems **14** (1998) 339–353. Printed in the UK PII: S0266-5611(98)87954-9

Exterior and limited-angle tomography in non-destructive evaluation

Eric Todd Quinto†
Department of Mathematics, Tufts University, Medford, MA 02155, USA

Received 25 September 1997, in final form 8 December 1997

Abstract. The author's exterior reconstruction algorithm is used to reconstruct two high-quality finely sampled exterior tomographic data sets from a high-resolution cone beam computed tomography scanner developed by Perceptics, Inc. One data set is complete exterior data and the other data set is limited-angle exterior data with an angular range of 135°. The author adapts his algorithm to reconstruct this limited-angle data set. Reconstructions are also made from two subsets of this data set: a highly limited-angle data set with an angular range of 30°, and a data set with sparser data ($\frac{1}{32}$ of the original data). A description of the inversion algorithm and a continuity estimate (stability bound) for the algorithm are given.

1. Introduction

X-ray computed tomography (CT) is an important, effective modality to find the densities of objects, and it has revolutionized diagnostic radiology and non-destructive evaluation. Typically, the object to be imaged is placed in a scanner and x-rays are taken over fairly uniformly distributed lines passing through all parts of the object. Such data are called *complete tomographic data*. Because the internal structure of an object is precisely shown in its CT reconstruction, radiologists can detect tumors in the body non-invasively and engineers can assess the magnitude and nature of defects in industrial objects. X-ray CT has been shown to be effective for the non-destructive evaluation of rocket parts [1, 2].

However, there are cases in which a complete data set is not efficient to use or even possible to acquire. In these cases, standard tomographic reconstruction algorithms [3] will not be usable because they require complete data. The data acquired in such cases are called *limited* tomographic data. One aim of this article is to show the utility of the author's exterior reconstruction algorithm for limited data tomography in industrial CT. Tests of the algorithm on two high-quality data sets provided by Perceptics, Inc., a subsidiary of Westinghouse, will be given. One of the data sets is limited-angle exterior data det with a range of 135°. To test the limits of the algorithm, reconstructions are made from two subsets of this data set: a highly limited-angle data set with an angular range of 30°, and a data set with sparser data ($\frac{1}{32}$ of the original data).

Exterior tomographic data are data given on lines that do not pass through the centre of an object. Exterior data result when the object is so large that x-rays cannot penetrate the centre of the object. This occurs in the non-destructive evaluation of large rocket motors because of their large diameter; x-rays cannot penetrate their centres. Reconstruction algorithms using exterior data have advantages. Data acquisition time will be lower than

† E-mail address: equinto@math.tufts.edu

0266-5611/98/020339+15$19.50

with normal CT scans because less data are required; on large diameter rocket motors, the acquisition time for standard CT data can be 100 minutes or longer for a single slice [4]. Furthermore, high-density objects and data artefacts from inside the rocket do not affect reconstructions using exterior data; although they do affect reconstructions using standard algorithms that require these interior data. Smaller exterior CT scanners can be designed to work on-site because of the smaller amount of data to be acquired. The Challenger tragedy demonstrates the utility of such on-site scanners for detecting defects in rocket motors. Exterior data are also useful for astronomical studies of the solar corona [5] and in medical tomography [6, 7]. Of course, inversion from exterior data does not reconstruct the centre of the object, which is not imaged.

Helgason [8] proved the exterior problem is solvable for rapidly decreasing functions on $\mathbb{R}^n$. Cormack developed an inversion formula for exterior data for compactly supported functions [9]. Lewitt and Bates [10, 11], Louis and Rieder [12, 13], and Natterer [7] have developed effective reconstruction algorithms that use exterior data. Lewitt and Bates' and Louis' algorithms complete the data by projecting it onto the range of the Radon transform with complete data and then using a standard inversion method.

The author's *exterior reconstruction algorithm* (ERA) [14, 15, 16] reconstructs from exterior data. It employs a singular value decomposition ([17]; [14] for $\mathbb{R}^n$) and *a priori* information about the shape of the object to be reconstructed. Specifically it uses the fact that the part of the object of interest is an annulus of known radius. The algorithm will be outlined in section 2 and its stability will be analysed in section 4.

Limited-angle tomographic data are data over lines in a limited angular range. Limited-angle data result when the CT scanner cannot rotate completely around the object. This occurs in electron microscopy because the microscope can only obtain a limited angular range of usable data. Limited-angle data also are used in industrial tomography when the scanner cannot acquire data for lines all around the object.

Limited-angle exterior data are data that are both exterior and of limited angular extent. Such data would result when an object is so big that exterior data must be taken and a CT scanner cannot x-ray all around the object or when some part of the exterior annulus of the object is impenetrable to x-rays. Theorem 2.2 of Boman and Quinto [18] shows that inversion from limited-angle exterior data is possible (this transform is injective). The author has developed his ERA for limited-angle exterior data, and reconstructions from such data are presented in section 3.

Common defects in rocket exit cones and rocket motors are of the same general shape. Many rocket exit cones are made up of 40 or more laminated layers, and delaminations (very thin separations that run between the layers) are typical defects. A rocket motor is made up of a metal or composite shell that surrounds a thin insulating layer that surrounds rocket fuel. Tiny air pockets on either side of the insulator or separations in composite cases or gaskets are common defects that need to be found. These defects occur along the outer circumference of the motor, and the centres of rocket motors are often not of structural interest. For both rocket motors and exit cones, the most important sections to evaluate are typically the outer parts of the object, annular rings (as seen in cross section). Furthermore, the typical defects are separations with sharp boundaries in the radial direction [2, 1]. There are mathematical reasons why exterior data are ideally suited to detect such defects [19] (see the discussion in section 3.2).

Reconstruction from limited-angle data [13, 20–23] or from exterior data is much more highly ill-posed (that is, much more difficult and more sensitive to noise) than standard tomography. In fact, reconstruction from limited-angle or exterior data is continuous in no range of Sobolev norms. By comparison, reconstruction with complete data is continuous of

order $+\frac{1}{2}$ in Sobolev norms. One other effective approach for limited data CT problems is local CT [24–27] in which one reconstructs the location of singularities rather than density values. An analysis in Sobolev spaces of the stability of reconstruction from limited x-ray CT data is given in [19].

Section 2 of this article outlines the author's ERA. Reconstructions and a discussion are in section 3. An analysis of algorithm stability is given in section 4.

2. The mathematics of the exterior reconstruction algorithm

2.1. The basic algorithm

The algorithm is outlined here to give perspective on the reconstructions and because it will be used in the proof of the stability result in section 4.

In this section, we will use parallel-beam geometry because the theorems are easier to state in this case. Let $\cdot$ denote the standard inner product on $\mathbb{R}^2$; let $|\ |$ be the norm, and let $\mathrm{d}x$ be the Lebesgue measure on $\mathbb{R}^2$. Let $\theta \in [0, 2\pi]$, and let $p \in \mathbb{R}$. Now let $\mathrm{d}\theta$ and $\mathrm{d}p$ denote the standard measures on $[0, 2\pi]$ and $\mathbb{R}$, respectively. The line $L(\theta, p) = \{x \in \mathbb{R}^2 | x \cdot \bar{\theta} = p\}$ has normal vector $\bar{\theta} = (\cos\theta, \sin\theta)$ and directed distance p from the origin. The points (θ, p) and $(\theta + \pi, -p)$ parametrize the same line $L(\theta, p)$, so we will always assume $p \geqslant 0$ in this article. Let $\mathrm{d}x_L$ be an arc length on $L(\theta, p)$. The *classical Radon transform* is defined for an integrable function f on $\mathbb{R}^2$ by

$$Rf(\theta, p) = \int_{L(\theta,p)} f(x)\,\mathrm{d}x_L. \tag{2.1}$$

This is just the integral of f over the line $L(\theta, p)$.

Let E be the exterior of the unit disk in $\mathbb{R}^2$, $E = \{x \in \mathbb{R}^2 | 1 \leqslant |x|\}$. E represents the part of an object to be reconstructed with exterior CT data; the unit disk is the centre that will not be reconstructed. Let $E' = [0, 2\pi] \times [1, \infty)$. E' corresponds to the set of lines $L(\theta, p)$ that lie in E, the set of lines used in exterior data.

The *exterior Radon transform* is the transform R as a map from integrable functions on E, the area outside the centre of the object to be reconstructed, to integrable functions on E', the set of lines that do not meet the centre of the object. Let $L^2(E)$ be the Hilbert space of functions on E defined by weight $(1/\pi)|x|(1 - |x|^{-2})^{1/2}\,\mathrm{d}x$ and let $L^2(E')$ be the Hilbert space of functions on E' defined by weight $(\pi p)^{-1}\mathrm{d}\theta\mathrm{d}p$.

For $\alpha > -1$ and for $\beta > -1$ and m a non-negative integer, the shifted Legendre polynomials $\{Q_m(\alpha, \beta, t) | m = 0, 1, 2, \ldots\}$ on $[0, 1]$ are defined by the positivity condition

$$\int_0^1 t^m Q_m(\alpha, \beta, t) t^\alpha (1 - t)^\beta\,\mathrm{d}t > 0$$

and the orthogonality relation

$$\int_0^1 Q_m(\alpha, \beta, t) Q_n(\alpha, \beta, t) t^\alpha (1 - t)^\beta\,\mathrm{d}t = \delta_{mn}$$

where $Q_m(\alpha, \beta, t)$ is a real-valued polynomial of degree m in t and δ_{mn} is Kronecker's delta. Let $\ell \in \mathbb{Z}$ and $m \geqslant 0$. To give our singular value decomposition (SVD) we need the following functions,

$$\begin{aligned} f_{\ell m}(r) &= r^{-2} Q_m(-0.5, 0.5, r^{-2}) \qquad \text{for } \ell \text{ even} \\ f_{\ell m}(r) &= r^{-3} Q_m(0.5, 0.5, r^{-2}) \qquad \text{for } \ell \text{ odd} \\ g_{\ell m}(p) &= p^{-(|\ell|+1)} Q_m(|\ell|, 0, p^{-2}). \end{aligned} \tag{2.2}$$

One part of the author's algorithm is the following SVD (see [17, 14] and [15, propositions 3.1–2]). Note that $[\ell/2]$ is the greatest integer less than or equal to $\ell/2$.

Proposition 2.1. *Define* $F_{\ell m}(r\bar{\theta}) = f_{\ell m}(r)\mathrm{e}^{\mathrm{i}\ell\theta}$, *and let* $G_{\ell m}(\theta, p) = g_{\ell m}(p)\mathrm{e}^{\mathrm{i}\ell\theta}$. *Then,* $\{F_{\ell m}|\ell \in \mathbb{Z},\ m \geqslant 0\}$ *is an orthonormal basis of* $L^2(E)$, *and* $\{G_{\ell m}|\ell \in \mathbb{Z},\ m \geqslant 0\}$ *is an orthonormal basis of* $L^2(E')$. *Furthermore, the exterior Radon transform* $R : L^2(E) \to L^2(E')$ *satisfies*

$$RF_{\ell m}(\theta, p) = 0 \qquad \text{for } m < [|\ell|/2] \tag{2.3a}$$

and

$$RF_{\ell m}(\theta, p) = C_{\ell m'}G_{\ell m'}(\theta, p) \qquad \text{for } m \geqslant [|\ell|/2] \text{ where } m' = m - [|\ell|/2], \tag{2.3b}$$

and

$$C_{\ell m'} = \frac{\sqrt{2\pi}}{\sqrt{|\ell| + 2m' + 1}}. \tag{2.4}$$

Recall that the null space of this transform is the set of all $f \in L^2(E)$ with $Rf = 0$. By proposition 2.1, (2.3*a*), this null space is the closure of the span of all functions $F_{\ell m}$ for $|\ell| > 1$ and $m < [|\ell|/2]$.

Notation. *A generic function in the null space of the exterior transform (in the closure of the span of* $\{F_{\ell m}|m < [|\ell|/2]\}$*) will be denoted* f_N. *A generic function in the orthogonal complement of this null space (in the closure of the span of the* $\{F_{\ell m}|m \geqslant [|\ell|/2]\}$*) will be denoted* f_R. *When discussing a given function* $f \in L^2(E)$, *then* f_N *will denote some projection of* f *onto the null space and* f_R *will denote some projection onto the orthogonal complement. Finally,* f_ℓ *will denote the* ℓ*th polar Fourier coefficient of* f,

$$f_\ell(r) = \frac{1}{2\pi}\int_{\theta=0}^{2\pi} f(r\bar{\theta})\mathrm{e}^{-\mathrm{i}\ell\theta}\,\mathrm{d}\theta. \tag{2.5}$$

An immediate corollary of the expression for the singular functions is the null-space characterization [14]:

Proposition 2.2. *A function* $f_N \in L^2(E)$ *is in the null space of* $R : L^2(E) \to L^2(E')$ *if and only if, for each* $\ell \in \mathbb{Z}$, *the* ℓ*th polar Fourier coefficient,* $(f_N)_\ell(r)$ *is a polynomial in* $1/r$ *of the same parity as* ℓ, *of degree at most* $|\ell|$, *and with lowest order term in* $1/r$ *of degree at least* 2. *Therefore,* $(f_N)_0 = (f_N)_{\pm 1} = 0$.

Let $\mathcal{N}_\ell$ *be the space of polynomials in* $1/r$ *that are* ℓ*th Fourier coefficients of null functions. Note that* $\dim \mathcal{N}_\ell = [|\ell|/2]$.

Let $f(x) \in L^2(E)$ be the density to be reconstructed. The SVD gives f_R, the projection of f onto the orthogonal complement of the null space of the exterior Radon transform. Because of the slow decrease of singular values in (2.4), recovering f_R is only as mildly ill-posed as inversion of the Radon transform with complete data (cf the singular values in [28]).

Following the notation above, let f_N be the projection of f onto the null space of the exterior transform. Of course, $f = f_R + f_N$ and f_N is not recovered by the SVD.

The second key to the algorithm is the fact that rocket bodies and exit cones have *a priori* known exterior radius $R_{\text{big}} > 1$ and also a relatively homogeneous inner structure. So, one knows $f(x) = 0$ for $|x| > R_{\text{big}}$, that is, f is zero for x outside the rocket. One also

assumes $f(x)$ is constant near $|x| = 1$. By this assumption, $f(r\bar{\theta})$ is constant for $r \approx 1$ and all θ. So, the polar Fourier coefficients of f for $\ell \neq 0$ are all zero near $r = 1$:

$$f_\ell(r) = 0 \qquad \text{for } r \approx 1 \text{ and } \ell \neq 0. \tag{2.6}$$

For rocket exit cones, this assumption, (2.6) can be made exact; by scaling properly, $|x| \approx 1$ can be chosen just inside the inner boundary of the exit cone, and $f(x) = 0$ for $|x| \approx 1$. For rocket bodies, even if the density of the area containing rocket fuel is not constant, it is often homogeneous enough so that (2.6) can be used by the algorithm. In the reconstructions in section 3, the density is not exactly constant near the inner boundary, and the reconstructions are good. The algorithm has been successfully tested on simulated data with a density difference of 50% near $r = 1$ [15].

This *a priori* information is used to recover f_N. Because each basis function is expressed in terms of an $e^{i\ell\theta}$, the algorithm is performed on each Fourier coefficient. We can assume $|\ell| > 1$ by proposition 2.2. As we assume f is constant in a small interval $[1, R_{\text{small}}]$ where $R_{\text{small}} \approx 1$, and as $f = f_N + f_R$, the *a priori* condition (2.6) becomes

$$(f_N)_\ell(r) = -(f_R)_\ell(r) \text{ for } r \in [1, R_{\text{small}}] \cup [R_{\text{big}}, \infty). \tag{2.7}$$

This restriction uniquely determines $(f_N)_\ell$ for $r \geqslant 1$ because $(f_N)_\ell$ is a polynomial in $1/r$.

The ERA recovers f_ℓ by first using the SVD to recover $(f_R)_\ell(r)$ for $r \geqslant 1$ and then using equation (2.7) and the null space restriction, proposition 2.2, to find $(f_N)_\ell(r)$. A polynomial in $\mathcal{N}_\ell$ (proposition 2.2) is a least-square fit to the data, $-(f_R)_\ell(r)$, for $r \in [1, R_{\text{small}}] \cup [R_{\text{big}}, \infty)$.

For the reconstructions in section 3, $R_{\text{small}} = 1.01$ and $R_{\text{big}} \approx 1.06$, and this polynomial, the reconstruction for $(f_N)_\ell$, is interpolated to $[R_{\text{small}}, R_{\text{big}}]$ (see section 4). This gives the reconstruction of the Fourier coefficient f_ℓ, and the reconstruction of f is the sum of the Fourier coefficients. The difficult part of the reconstruction is finding $(f_N)_\ell$. Since the problem is so highly ill-posed, every algorithm must involve some regularization and most of the regularization in the ERA is in the reconstruction of $(f_N)_\ell$.

2.2. The interpolation for limited-angle data

The limited-angle exterior data from the Perceptics data set in section 3.1 were interpolated to become complete exterior data usable for the ERA. It is easier to describe the interpolation using a type of fan-beam geometry. The Perceptics scanner is a cone beam with one fixed source and fixed detectors, and the object rotates on a turntable inside the scanner. Let θ be the angle of rotation of the object and let j be the detector number. Now, let f be the function or density to be reconstructed. So, $Rf(\theta, j)$ is the data (Radon transform) of f at the jth detector when the source is at position θ, now expressed in degrees.

The ERA needs data $Rf(\theta, j)$ for all detectors j and for all θ around the circle from 0° to 360°, but the given data had sources in a range $0^\circ \leqslant \theta \leqslant 135.3^\circ$. Data were filled in the missing range, $135.3^\circ \leqslant \theta \leqslant 360^\circ$ using linear interpolation in θ for each fixed j.

This type of data extension will work with any data set that is limited in angular extent. The inversion methods for limited angular data of [10, 29, 22] project the data onto a function in the range of the Radon transform with complete data. The ERA projects onto the range of the exterior Radon transform when it calculates the singular values. So, even though the linearly interpolated function is probably not in the range of the Radon transform, it will be put in the range in this projection step. Perhaps this projection step helps the algorithm work well with this doubly limited data.

3. Reconstructions and discussion

Two Perceptics data sets are reconstructed, one that is limited-angle exterior data (section 3.1) and the other that is complete exterior data (data not limited in angular extent) (section 3.2).

3.1. Limited-angle exterior data

This data set was taken by a Perceptics fan-beam scanner with one source and evenly spaced fixed detectors. The object is rotated on a turntable in 1353 equi-angular positions between $\theta = 0$ and 135.3°. The object had an outer radius $r = 36.6$ in and data were given for lines outside the disk of radius $r = 34.74$ in. Then, 281 detectors were used in the reconstructions in figures 1(a) and (b).

Using the notation of theorem 2.1, the reconstruction shown uses $|\ell| \leqslant 600$ polar Fourier coefficients (and to make smoother reconstructions, only coefficients for $|\ell| \leqslant 100$ are used very near the inside boundary, $r = 34.74''$). Reconstructions using few polar Fourier coefficients were also made, and the boundaries are not quite as sharp. Three hundred polynomials are summed for each Fourier coefficient ($m' \leqslant 300$ in proposition 2.1).

For each of the first 30 Fourier coefficients, the first ten null-space terms were summed, and this was used as the null-space component of the reconstruction (using the notation of theorem 4.1 $m_{\min} = 10$ and the sum included the $\tilde{f}_{\ell m}$ for $|\ell| \leqslant 30, m < \min(10, [|\ell|/2])$). Without this smoothing (setting high-frequency null-space terms to zero) the errors in f_N would cause angular oscillations that would make the reconstruction useless (creating large 'bumps' in the reconstruction at equally spaced angles, corresponding to inaccurate values for null-space coefficients). Theorem 4.1 and (4.2c) provide a continuity estimate for the projection on the null space.

Overall, the boundaries are clear and the small blobs inside the propellant are quite clear with good density resolution. The shell and propellant densities are fairly uniform. The only feature of the object which is not completely clear is a possible separation near the boundary of the rocket at around 20°. This is visible in the reconstruction, but it is smoothed out in both radius and angular extent. Rather than looking like a sharp separation, it looks like a small indentation. In order to provide sufficiently fine radial resolution, the scale in r is magnified (by a factor of 27), and this makes separations smoother than they would appear if shown to scale. However, one could not see the small details, if the reconstruction were displayed to scale.

The reconstruction in figure 1(b) uses a subset of this data with only a 30° range of sources ($\theta = 60$–90°) and all other parameters are the same. The reconstruction is essentially identical to that in figure 1(a) for the region imaged and reconstructed.

Reconstructions were also made with fewer source positions and fewer detectors. The reconstructions were satisfactory when one used every second source position and every second detector—one fourth of the original data. In figure 1(c) is a reconstruction with every eighth source position and every fourth detector. The image is degraded and there are annoying 'brush stroke' artefacts, but the structure is visible even though $\frac{1}{32}$ of the data in figure 1(a) are used. Four hundred Fourier coefficients are reconstructed with 169 source positions (effectively 450 source positions in $[0, 360^\circ]$ after extrapolation) and 70 detectors.

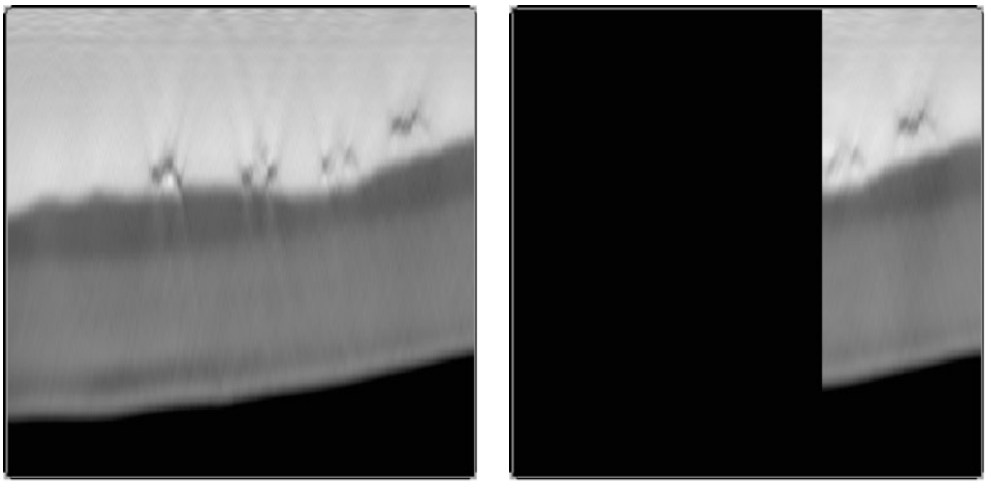

(*a*) (*b*)

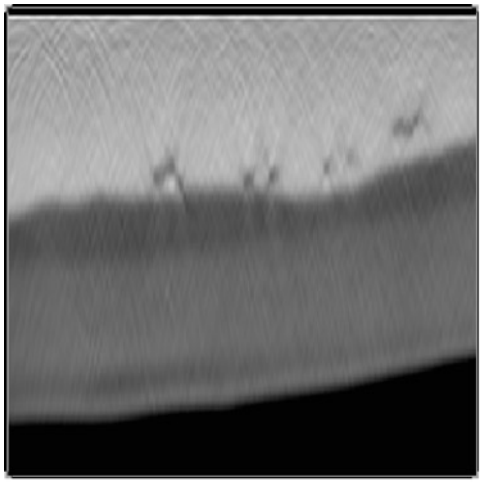

(*c*)

Figure 1. (*a*) Polar coordinate display of an ERA reconstruction from a 135° angular range limited-angle exterior data set of a Perceptics rocket motor mock-up (section 3.1). The horizontal axis corresponds to $\theta \in [0^\circ, 90^\circ]$, the vertical corresponds to $r \in [34.74, 36.75]$ (magnified by a factor of 27). The bottom of the picture shows some area outside the object. The part of the reconstruction in $[90^\circ, 135.3^\circ]$ is of the same quality but less interesting. (*b*) Polar coordinate display of an ERA reconstruction from a 30° angular range limited-angle exterior data set of the Perceptics rocket motor mock-up in (*a*). The data only include sources from $\theta = 60^\circ$ to 90° from the data set used in (*a*). The reconstruction is given in this same angular range, the range that is determined by these restricted data. The scale is as in (*a*). (*c*) Polar coordinate display of an ERA reconstruction of the Perceptics rocket motor mockup in (*a*) using $\frac{1}{32}$ the data used in (*a*). The scale is as in (*a*).

3.2. Complete exterior data

This data set was taken by a Perceptics fan-beam scanner with one source and evenly spaced detectors. The object was rotated on a turntable a full 360°. The object had outer radius $r = 37.2$ in and data were given for lines outside the circle of radius $r = 32.55$ in.

However, the region of interest was the annulus with inner radius $r = 35.46$ in and only data for lines outside $r = 35.46$ in were used in the reconstruction. 1800 source positions and 390 detectors were used in the reconstructions in figure 2. Reconstruction with all data (lines outside the circle with radius 32.55 in) resulted in blurrier boundaries between regions, probably because the algorithm, including the interpolation procedure described in section 2.1, had to be carried out over a longer interval, $[R_{\text{small}}, R_{\text{big}}]$.

A limitation in data preprocessing created a band of high density that masked about $\frac{1}{6}$ of the reconstruction. This was perhaps due to miscalibration of the detector response for certain detectors, and it was practically uniform over the source positions. Therefore, a simple postprocessing in the $\ell = 0$ Fourier coefficient was used to improve the reconstruction.

Using the notation of theorem 2.1, the reconstruction shown uses $|\ell| \leqslant 600$ polar Fourier coefficients (and to make smoother reconstructions, only coefficients for $|\ell| \leqslant 100$ are used very near the inside boundary, $r = 35.46$ in). Three hundred polynomials are summed for each Fourier coefficient ($m' \leqslant 300$ in proposition 2.1). For each of the first 30 Fourier coefficients, the null-space terms were summed and this was used as the null-space component of the reconstruction (using the notation of section 4, $\tilde{f}_{\ell m}$ for $|\ell| \leqslant 30,\ m < [|\ell|/2]$).

There are two high-density objects in the rocket propellant at about radius $r = 34$ in that are visible in reconstructions that use the entire data. These created artefacts in the ERA reconstruction that uses all the data, and probably would create problems for other reconstruction methods. Since the ERA reconstructions of the region of interest do not need these inside data that caused the streaks, these reconstructions do not suffer from such streaks.

Both of the original Perceptics data sets are cone beam data sets, that is, data sets with sources on a circle but detectors in a two-dimensional array. The midplane is the plane of the sources, and the ERA is a planar CT algorithm. Only data over lines in that plane are genuinely planar CT data. However, it is important to image data off that midplane. Therefore, both Perceptics data sets are data for a two-dimensional set of lines that were at

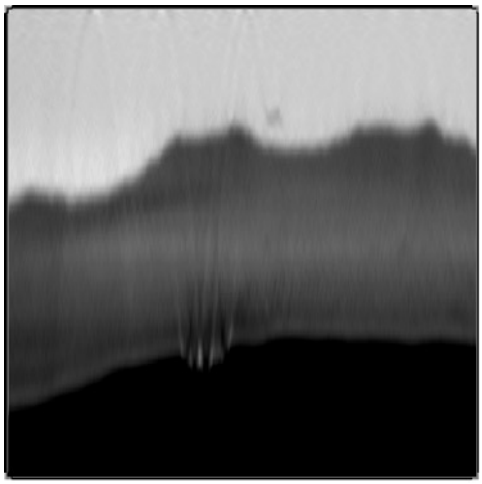

Figure 2. Polar coordinate display of an ERA reconstruction from complete exterior data of a Perceptics rocket motor mock-up (section 3.2). The horizontal axis corresponds to $\theta \in [0^\circ, 180^\circ]$, the vertical corresponds to $r \in [35.46, 37.2]$ (magnified by a factor of 50).

least 4 in above the midplane (and perhaps as much as 10 in). This causes no apparent ill effects and there are no artefacts or distortions attributable to this.

The *tangent casting effect* [2, p 78] associated with sharp material density differences that occur tangent to x-rays in the data set can be used to evaluate tomographic reconstructions. Simply put, an x-ray that travels tangent to a defect will detect it easily. This is true mathematically because of an analytic property of the Radon transform; the Radon transform easily detects boundaries of f that are tangent to lines in the data set, but not boundaries in other directions. The rigorous mathematical reason for this analytic property is that R is an elliptic Fourier integral operator of a special form (this discussion has been made precise in [19] using microlocal analysis). This methodology helps explain why the pictures in section 3.1 show detail inside the shell that is fine enough to require magnification in r (by 27 times in figures 1(a)–(c)), even though the data are so limited; most of the boundaries are tangent to lines in the data set. In figure 2, the epoxy raceway adhesive track at the boundary of the rocket is a little distorted. The outer boundary of the rocket is easy for exterior data to detect since lines tangent to it are in the exterior data set, and it is reconstructed well. However, tangents to the 'vertical' boundaries of the track go through the centre of the object and are not in the exterior data set. Therefore, the track is harder to reconstruct from exterior data than the other features in the object.

4. Stability analysis

In this section, we will give an inverse continuity theorem for the algorithm. This inverse continuity estimate is proven for the actual numerical methods used for the reconstructions in section 3.

We will not give a bound on error between reconstruction and original object for two reasons. As implemented, only lower-order coefficients of f_N are reconstructed, not f_N itself (this is because the step to find f_N requires the most regularization). Furthermore, the accuracy estimates for numerical integration require the data to be fairly smooth or in high Sobolev spaces, but the data being reconstructed have large Sobolev norms because of the density changes at boundaries.

To decrease Gibbs' phenomenon in the polynomial sums for the reconstruction, the algorithm multiplies the coefficients of the basis polynomials in r by weight factors when it sums them up, much like in Cesaro sums. The factor for the 'range' reconstruction, $(f_R)_\ell$, is denoted $c_R(m)$ (see the first footnote to example 4.2 below) and the sum for $(f_R)_\ell$ is given in (4.8) below. The factor for the null-space reconstruction, $(f_N)_\ell$, is $c_N(\ell, m)$ (see the last two footnotes to example 4.2) and the sum for $(f_N)_\ell$ is given in (4.12).

We let

$$\{\tilde{f}_{\ell m}(r) | m = 0, \ldots, [|\ell|/2] - 1\} \tag{4.1}$$

be a basis of the space $\mathcal{N}_\ell$ (see proposition 2.2) that is orthonormal on $[1, R_{\text{small}}] \cup [R_{\text{big}}, \infty)$ with weight $2r^2\sqrt{1 - r^{-2}}$.

Theorem 4.1. *Let $g : [0, 2\pi] \times [1, R_{\text{big}}] \to \mathbb{R}$ be a bounded, measurable function, and let $\|g\|_\infty$ be the sup norm of g. Let $R^{-1}g$ denote the ERA inversion of g using the $G_{\ell m}$ for $|\ell| \leqslant \ell_0$ and $m \leqslant m_{\max}$ and the numerical methods outlined in section 2 and below. We assume ℓ_0 is less than the number of source positions.*

Then,

$$\|R^{-1}g\|_{L^2(E)} \leqslant \left(\max_{|\ell| \leqslant \ell_0} (E_R(\ell)(1 + E_N(\ell)))\|\chi_{[1, R_{\text{big}}]}\|_{(q_k)}\right)\|g\|_\infty \tag{4.2a}$$

where

$$E_R(\ell) = \max_{m \leqslant m_{\max}} \left(\frac{c_R(m)}{C_{\ell m}} \right) \tag{4.2b}$$

and

$$E_N(\ell) = \max_{m < [|\ell|/2]} \left(c_N(\ell, m) \left[\min(m_{\min}, [|\ell|/2]) \int_{[1, R_{\text{big}}]} \tilde{f}^2_{\ell m}(r) r^2 \sqrt{1 - r^{-2}} \, \mathrm{d}r \right]^{1/2} \right). \tag{4.2c}$$

Here, $\|\chi_{[1,R_{\text{big}}]}\|_{(q_k)}$ is the quadrature norm defined above (4.4) *of the characteristic function of $[1, R_{\text{big}}]$ and $C_{\ell m}$ is the singular value given in proposition 2.1. The function $c_R(m)$ (first footnote below) is the convolution factor for the sum for $(f_R)_\ell$ in (4.8). The function $c_N(\ell, m)$ (second footnote below and that on the next page) is the convolution factor that the null functions $\tilde{f}_{\ell m}$ are multiplied by in the sum for f_N in (4.12). We let $m_{\min} \leqslant m_{\max}$ and assume $c_N(\ell, m) = 0$ for $m \geqslant m_{\min}$. We assume that the data are taken on a rotation invariant fan-beam (or parallel beam) grid and that R_{big} is large enough that supp g is inside the circle $r = R_{\text{big}}$ and g is zero at the outermost detector.*

This theorem can be applied to limited-angle exterior data that are extended as proposed in section 2.2. The reason is that the L^∞ norm of the linear extension is the same as the L^∞ norm of the original data.

Example 4.2. The continuity estimate from theorem 4.1 for the reconstructions in section 3 is now given; the max term in (4.2*a*) is calculated and the regularization parameters $m_{\max}$, $m_{\min}$ and c_R and c_N are given.

For all reconstructions $m_{\max} = 300$ and $c_R(m)$ is a smooth function that is identically one on $\{0, 1, \ldots, 120\}$ and then decreases smoothly to zero at $m_{\max}$†. The null-space regularizer, $c_N(\ell, m)$ is different for each case and will be given below. Because the null space is spanned by $F_{\ell m}$ for $|\ell| > 1$ and $0 \leqslant m < [|\ell/2|]$ (see (2.3*a*)), the only values of $c_N(\ell, m)$ that affect the regularization are for (ℓ, m) in this set of indices.

As noted below theorem 4.2, we can use the estimates in theorem 4.1 for the limited-angle reconstructions in section 3.1. For the reconstruction in figure 1(*a*), $\ell_0 = 600$, $R_{\text{big}} = 1.058$ (if the inner radius is 1) and $m_{\min} = 10$. The function $c_N(\ell, m)$ is identically zero for $|\ell| > 30$. For $|\ell| \leqslant 30$, $c_N(\ell, m)$ is identically one for $m \in \{0, \ldots, 5\}$ and decreases smoothly to zero at $m_{\min} = 10$‡. This means that the null-space coefficients $(f_N)_\ell$ were added up to $|\ell| = 30$, and for these, $m_{\min} = 10$ ($\tilde{f}_{\ell m}$ for $|\ell| \leqslant 30$ and $m < \min([|\ell|/2], 10)$). The maximum norm according to theorem 4.1 is 10.0. This maximum norm bound occurs at $\ell = 30$. If no null functions were used, the maximum norm bound would be 3.9, and it would occur at $\ell = 600$. For the reconstruction in figure 1(*b*), all the constants and regularizations are the same as in the reconstruction in figure 1(*a*), so the bounds are the same. For the reconstruction in figure 1(*c*), $\ell_0 = 400$ but all other regularization constants are the same as the reconstruction in figures 1(*a*) and (*b*), so the bound is the same, 10.0, since the maximum bound occurs at $\ell = 30$.

For the reconstruction in figure 2, $m_{\max} = 300$, $\ell_0 = 600$, $m_{\min} = 15$, and $R_{\text{big}} = 1.05$. The function $c_N(\ell, m)$ is identically zero for $|\ell| > 30$. For $|\ell| \leqslant 30$, $c_N(\ell, m)$ is identically one for $m \in \{0, \ldots, 10\}$ and decreases smoothly to zero at $m = 20$§. This means that the null space coefficients $(f_N)_\ell$ were added up to $|\ell| = 30$, and for these, all null basis functions were used ($\tilde{f}_{\ell m}$ for $|\ell| \leqslant 30$ and $m < [|\ell|/2]$). The function c_N in this experiment

† Specifically, for $m \in \{121, \ldots, 300\}$, $c_R(m) = h((300 - m)/180)$ where $h(x) = (3x^2 - 2x^3)$.

‡ Specifically, for $m \in \{6, 7, 8, 9, 10\}$ and $|\ell| \leqslant 30$, $c_N(\ell, m) = h((10 - m)/5)$ where $h(x)$ is given above.

§ Specifically, for $m \in \{10, 11, \ldots, 20\}$ and $|\ell| \leqslant 30$, $c_N(\ell, m) = h((20 - m)/10)$ where $h(x)$ is given above.

is less regularizing than in the limited-angle experiments. This maximum norm bound occurs at $\ell = 30$. The maximum norm bound according to theorem 4.1 is 21.6. If one were to reconstruct using $m_{\min} = 10$, and c_R and c_N as in section 3.1, then the bound would be 8.6. If no null functions were used, the bound would be 3.6.

The reconstructions shown in section 3 are much better than these norms indicate. This is true, in large part, because of the high-quality low-noise data, and because the middle and high polar Fourier coefficients of the data are at least two orders of magnitude smaller than the lower coefficients. For example, the maximum of the singular values occurs at $\ell = 600$, but the data are concentrated in Fourier coefficients $|\ell| \leqslant 50$. This is not surprising for rocket data, as is discussed in section 3.2. If the data were noisier or more of the details were concentrated in high polar Fourier coefficients, then stronger regularization would have been used. For example, the c_R and c_N would have been chosen to go to zero more quickly.

Proof of theorem 4.1. The proof will be done in four steps. We take the data $g(\theta, p)$ parametrized in parallel beam geometry and given on a rotation invariant grid, and we bound above the result of each part of the algorithm on g. Note that the $g_{\ell m}(p)$ are orthonormal with measure of integration $(2/p)\,\mathrm{d}p$ on $[1, \infty)$ and, of course, the $\mathrm{e}^{\mathrm{i}\ell\theta}$ are orthonormal with measure $1/(2\pi)\,\mathrm{d}\theta$ on $[0, 2\pi]$.

(1) *Calculating the ℓth Fourier coefficient of g and doing linear interpolation.* Because the data are given on a rotation invariant fan beam grid, the function g is given on a grid that has fixed values of p_j, $j = 0, \ldots, n$ (corresponding to the different detectors that rotate around the object) and for each p_j, the grid in θ is $(\theta_i + \delta_j)$, $i = 1, \ldots, n'$, where (θ_i), $i = 1, \ldots, n'$ is an evenly spaced grid in $[0, 2\pi]$ that is rotated for each j by the factor δ_j [16].

First, the algorithm calculates the polar Fourier coefficients of g at the p_j for $|\ell| \leqslant \ell_0$. Because ℓ_0 is less than the number of source positions, the $\mathrm{e}^{\mathrm{i}\ell\theta}$, for $|\ell| \leqslant \ell_0$, are orthonormal on the evenly spaced grid $(\theta_i + \delta_j)$ and (equal) weights corresponding to the measure $1/(2\pi)\,\mathrm{d}\theta$. For these reasons, we can bound the sum

$$\sum_{|\ell| \leqslant \ell_0} |g_\ell(p_j)|^2 \leqslant \|g\|_\infty^2 \qquad \text{for each } j \tag{4.3}$$

because $\|g\|_\infty$ bounds the normalized discrete L^2 norm in θ of $g((\theta_i + \delta_j), p_j)$.

Next, the algorithm interpolates from the values of p_j defined by the detector positions to values q_k, $k = 0, \ldots, k'$ where k' is chosen to be greater than $m_{\max} + \ell_0$ and the q_k are chosen so that the orthogonal functions, $g_{\ell m}(p)$ in theorem 2.1 for $|\ell| \leqslant \ell_0$ and $m \leqslant m_{\max}$ are orthogonal on this finite grid (q_k) with weights corresponding to the measure $(2/p)\,\mathrm{d}p$. The nodes q_k and the quadrature weight are found as follows. One changes variable $t = 1/p^2$ and then, one chooses nodes t_k and appropriate weights for Legendre polynomial quadrature of degree k' on $[0, 1]$ and measure $\mathrm{d}t$. Then, one defines $q_k = 1/\sqrt{t_k}$. Because this quadrature rule on $[0, 1]$ is exact for polynomials up to order $2k' + 1$, the $g_{\ell m}(p)$ for $m \leqslant m_{\max}$ and $|\ell| \leqslant \ell_0$ are orthogonal on the grid (q_k) with the chosen weights.

For a function $h : [1, \infty) \to \mathbb{C}$, we let $\|h\|_{(q_k)}$ denote the discrete L^2 norm of h using these nodes (q_k) and associated weights. By evaluating the integral exactly, one sees that

$$\|\chi_{[1, R_{\mathrm{big}}]}\|_{(q_k)}^2 \approx 2 \ln R_{\mathrm{big}}. \tag{4.4}$$

Let $L(g_\ell)$ be this linearly interpolated function defined from $g_\ell(p_j)$. Because of (4.3) and since linear interpolation for points between each p_{j-1} and p_j is a convex combination

of $g_\ell(p_{j-1})$ and $g_\ell(p_j)$, we have

$$\begin{aligned}\sum_{|\ell|\leqslant\ell_0} |L(g_\ell)(q_k)|^2 &\leqslant \|g\|_\infty^2 \qquad \text{if } q_k \leqslant R_{\text{big}} \\ &= 0 \qquad \text{if } q_k > R_{\text{big}}.\end{aligned} \tag{4.5}$$

The equality in the second line of (4.5) is valid because we assume that $g(\theta_i + \delta_j, p_j)$ is zero for the largest p_j less than or equal to R_{big} and all i, and the linear interpolation is performed on $[p_j, p_{j+1}]$.

One application of (4.5) and the definition of $\| \ \|_{(q_k)}$ is the bound

$$\sum_{\ell\leqslant\ell_0} \|L(g_\ell)\|_{(q_k)}^2 \leqslant \|\chi_{[1,R_{\text{big}}]}\|_{(q_k)}^2 \, \|g\|_\infty^2. \tag{4.6}$$

Let f be the ERA inversion of g and then $(f_R)_\ell$ is the ℓth Fourier coefficient of the SVD inversion of g using proposition 2.1, and $(f_N)_\ell$ is the ERA reconstruction of the ℓth Fourier coefficient of the null-space component using proposition 2.2 and (2.7). The complete reconstruction of the ℓth Fourier coefficient, $L(g_\ell)$, by the ERA is:

$$f_\ell = (f_R)_\ell + (f_N)_\ell$$

and we estimate each part separately.

(2) *Estimating the norm of $(f_R)_\ell$ using the SVD.* Note that the $f_{\ell m}(r)$ are orthonormal on $[1, \infty)$ with measure $2r^2\sqrt{1-r^{-2}}\,\mathrm{d}r$.

The ERA uses quadrature on the q_k to calculate the coefficients of $g_{\ell m}(p)$, $Lg_\ell(p) \approx \sum_{m=0}^{m_{\max}} a_{\ell m} g_{\ell m}(p)$. Because the $g_{\ell m}(p)$ are orthonormal using quadrature on the nodes (q_k), we can bound

$$\sum_{m=0}^{m_{\max}} |a_{\ell m}|^2 \leqslant \|(Lg)_\ell\|_{(q_k)}^2. \tag{4.7}$$

The ERA as implemented includes the positive convolution factor $c_R(m)$ as regularizer in the calculation of $(f_R)_\ell$. The reconstruction of f_R using the SVD plus this factor is

$$(f_R)_\ell = \sum_{m=0}^{m_{\max}} c_R(m) \frac{a_{\ell m}}{C_{\ell m}} f_{\ell\,(m+[|\ell|/2])}. \tag{4.8}$$

Let $\|h(r)\|_{(r)}$ be the L^2 norm of $h : [1, \infty) \to \mathbb{C}$ in measure $2r^2\sqrt{1-r^{-2}}\,\mathrm{d}r$. Because the $f_{\ell m}(r)$ are orthonormal functions on $[1, \infty)$ with this weight, the norm of $(f_R)_\ell$ can be bounded above using (4.8) and (4.7) as follows

$$\begin{aligned}\|(f_R)_\ell\|_{(r)}^2 &= \sum_{m=0}^{m_{\max}} \left| c_R(m) \frac{a_{\ell m}}{C_{\ell m}} \right|^2 \leqslant \left(\max_{m\leqslant m_{\max}} \left(\frac{c_R(m)}{C_{\ell m}} \right)^2 \right) \sum_{m=0}^{m_{\max}} |a_{\ell m}|^2 \\ &\leqslant E_R^2(\ell) \|(Lg)_\ell\|_{(q_k)}^2\end{aligned} \tag{4.9}$$

where

$$E_R(\ell) = \max_{m\leqslant m_{\max}} \left(\frac{c_R(m)}{C_{\ell m}} \right). \tag{4.10}$$

(3) *Calculating $(f_N)_\ell$, the projection of $-(f_R)_\ell$ onto $\mathcal{N}_\ell$.* Recall that $\mathcal{N}_\ell$ is the set of polynomials in $1/r$ in proposition 2.2 that are ℓth Fourier coefficients of null functions. From (4.1) the set $\{\tilde{f}_{\ell m} | m = 0, \ldots, [|\ell|/2] - 1\}$ is a basis of $\mathcal{N}_\ell$ that is orthonormal on $[1, R_{\text{small}}] \cup [R_{\text{big}}, \infty)$ in measure $2r^2\sqrt{1-r^{-2}}\,\mathrm{d}r$.

Using (2.7) and proposition 2.2, we project $-(f_R)_\ell(r)$ onto $\mathcal{N}_\ell$ for $r \in [1, R_{\text{small}}] \cup [R_{\text{big}}, \infty)$ and $|\ell| \geqslant 2$. This will give the ERA reconstruction of $(f_N)_\ell$. For this purpose, let

$$b_{\ell m} = -\int_{[1,R_{\text{small}}]\cup[R_{\text{big}},\infty)} (f_R)_\ell(r)\,\tilde{f}_{\ell m}(r)\,2r^2\sqrt{1-r^{-2}}\,\mathrm{d}r \tag{4.11}$$

be the coefficient of $\tilde{f}_{\ell m}$ in the least-squares projection of $-(f_R)_\ell$ onto $\mathcal{N}_\ell$†. Since the $\tilde{f}_{\ell m}$ are orthonormal on this interval $[1, R_{\text{small}}] \cup [R_{\text{big}}, \infty) \subset [1, \infty)$,

$$\sum_{m=0}^{[|\ell|/2]-1} |b_{\ell m}|^2 \leqslant \|(f_R)_\ell\|^2_{(r)}.$$

Because the recovery of f_N is highly ill-posed, this part of the algorithm is regularized by using a convolution factor $c_N(\ell, m)$, with $c_N(\ell, m) = 0$, for $m \geqslant m_{\min}$. This convolved projection gives

$$(f_N)_\ell = \sum_{m=0}^{\min(m_{\min},[|\ell|/2])-1} c_N(\ell, m) b_{\ell m} \tilde{f}_{\ell m}. \tag{4.12}$$

The estimate for the norm of $(f_N)_\ell$ on $[1, R_{\text{big}}]$ uses Jensen's inequality [30, p 110] and the fact that the sum has at most $\min(m_{\min}, [|\ell|/2])$ terms because c_N is zero for $m \geqslant m_{\min}$:

$$\begin{aligned}\|\chi_{[1,R_{\text{big}}]}(f_N)_\ell\|^2_{(r)} &\leqslant M \sum_{m=0}^{M-1} |b_{\ell m}|^2 \int_1^{R_{\text{big}}} c_N^2(\ell, m)\,\tilde{f}^2_{\ell m}(r)\,2r^2\sqrt{1-r^{-2}}\,\mathrm{d}r \\ &\leqslant E_N^2(\ell)\|(f_R)_\ell\|^2_{(r)} \\ &\leqslant E_N^2(\ell)E_R^2(\ell)\|L(g_\ell)\|^2_{(q_k)} \text{ where } M = \min(m_{\min}, [|\ell|/2])\end{aligned} \tag{4.13}$$

and where

$$E_N(\ell) = \max_{m<[|\ell|/2]} \left(c_N(\ell, m) \left(\min(m_{\min}, [|\ell|/2]) \int_1^{R_{\text{big}}} \tilde{f}^2_{\ell m}(r)\,2r^2\sqrt{1-r^{-2}}\,\mathrm{d}r \right)^{1/2} \right). \tag{4.14}$$

Using (4.9) and (4.13), one sees that

$$\|((f_N)_\ell + (f_R)_\ell)\chi_{[1,R_{\text{big}}]}\|_{(r)} \leqslant (E_N(\ell) + 1)E_R(\ell)\,\|L(g_\ell)\|_{(q_k)}. \tag{4.15}$$

4.1. Bounding the final ERA inversion of g.

To bound the final inversion of g, we just add up the bounds (4.15) and use (4.6):

$$\begin{aligned}\|(f_N + f_R)\chi_{[1,R_{\text{big}}]}\|^2_{L^2(E)} &\leqslant \sum_{|\ell|\leqslant\ell_0} \left[(E_N(\ell) + 1)E_R(\ell)\right]^2 \|L(g_\ell)\|^2_{(q_k)} \\ &\leqslant \max_{|\ell|\leqslant\ell_0} [(E_N(\ell) + 1)E_R(\ell)]^2 \|\chi_{[1,R_{\text{big}}]}\|^2_{(q_k)} \|g\|^2_\infty\end{aligned} \tag{4.16}$$

This finishes the proof. □

† To implement this projection onto $\mathcal{N}_\ell$, one can choose nodes and weights on $[1, R_{\text{small}}]$ and $[R_{\text{big}}, \infty)$ such that the $\tilde{f}_{\ell m}$ are orthogonal with these nodes and weights and such that integration with respect to $2r^2\sqrt{1-r^{-2}}\,\mathrm{d}r$ for polynomials in $1/r$ (of sufficiently high degree) is exact using these nodes. (This is similar to the discussion between (4.3) and (4.4) for finding the (t_k) and (q_k) to integrate Lg.) Enough nodes must be chosen so that polynomial integration in each of the two subintervals is exact for products of $f_{\ell m}(r)$ and $\tilde{f}_{\ell\tilde{m}}$. In the algorithm, as implemented, a quadrature method with fewer nodes can be used, and it gives essentially the same results as the method outlined here.

Because the algorithm is stable under change in accuracy used in calculations (single to double to quadruple precision), round-off errors should be orders of magnitude less than $\|g\|_\infty$ in practice.

Acknowledgments

This article is the result of support by a subcontract to Perceptics, Inc. The Perceptics contract manager, Dr James Youngberg, was patient, flexible and supportive, and he was a man of his word. He was very helpful and forthcoming providing information about their data and experience with the problem as the author developed the algorithm for their data. The author is also indebted to Dr Paul Burstein of Skiametrics for much support and practical information. The author had many valuable conversations with Dr Adel Faridani and Dr Alfred Louis. He thanks Dr Christoph Börgers for his helpful comments on the article. The author is indebted to Dr Frank Wuebbling and the Institut für Numerische und instrumentelle Mathematik der Universität Münster for the display program for the figures. The author thanks the referees for useful comments that made the article clearer. The author was partially supported by NSF grants MCS 9123862 and 9622947.

References

[1] Schneider R J, Burstein P, Seguin F H and Kreiger A S 1986 High-spacial-resolution computed tomography for thin annular geometries *Review of Progress in Qualitative Non-destructive Evaluation* vol 5a, ed D O Thompson and D E Chimenti (New York: Plenum)

[2] Shepp L A and Srivastava S 1986 Computed tomography of PKM and AKM exit cones *AT&T Tech. J.* **65** 78–88

[3] Natterer F 1986 *The Mathematics of Computerized Tomography* (New York: Wiley)

[4] Burstein P 1989 Private communication

[5] Altschuler M D 1979 Reconstruction of the global-scale three-dimensional solar corona *Image Reconstruction From Projections, Implementation and Applications (Topics in Applied Physics 32)* ed G T Herman (Berlin: Springer) pp 105–45

[6] Shepp L A and Kruskal J B 1978 Computerized tomography: The new medical x-ray technology *Am. Math. Mon.* **85** 420–39

[7] Natterer F 1980 Efficient implementation of optimal algorithms in computerized tomography *Math Methods Appl Sci.* **2** 545–55

[8] Helgason S 1965 The Radon transform on Euclidean spaces, compact two-point homogeneous spaces, and Grassmann manifolds *Acta Math.* **113** 153–80

[9] Cormack A M 1963 Representation of a function by its line integrals with some radiological applications *J. Appl. Phys.* **34** 2722–7

[10] Lewitt R M and Bates R H T 1978 Image reconstruction from projections II. Projection completion methods (theory) 1978 *Optik* **50** 189–204

Lewitt R M and Bates R H T 1978 Image reconstruction from projections III. Projection completion methods (computational examples) *Optik* **50** 269–78

[11] Lewitt R M 1988 Overview of inversion methods used in computed tomography *Advances in Remote Sensing Retrieval Methods* (Hampton, VA: Deepak)

[12] Louis A 1988 Private communication

[13] Louis A and Rieder A 1989 Incomplete data problems in x-ray computerized tomography II. Truncated projections and region-of-interest tomography *Numer. Math.* **56** 371–83

[14] Quinto E T 1983 Singular value decompositions and inversion methods for the exterior Radon transform and a spherical transform *J. Math. Anal. Appl.* **95** 437–48

[15] Quinto E T 1988 Tomographic reconstructions from incomplete data—numerical inversion of the exterior Radon transform *Inverse Problems* **4** 867–76

[16] Quinto E T 1991 Computed tomography and rockets *Mathematical Methods In Tomography (Proc. Oberwolfach 1990) (Lecture Notes In Mathematics 1497)* (Berlin: Springer) pp 261–8

[17] Perry R M 1977 On reconstruction of a function on the exterior of a disc from its Radon transform *J. Math. Anal. Appl.* **59** 324–41
[18] Boman J and Quinto E T 1987 Support theorems for real analytic Radon transforms *Duke Math. J.* **55** 943–8
[19] Quinto E T 1993 Singularities of the x-ray transform and limited data tomography in $\mathbb{R}^2$ and $\mathbb{R}^3$ *SIAM J. Math. Anal.* **24** 1215–25
[20] Finch D 1985 Cone beam reconstruction with sources on a curve *SIAM J. Appl. Math.* **45** 665–73
[21] Lissianoi S 1994 On stability estimates in the exterior problem for the Radon transform *Lect. Appl. Math.* **30** 143–7
[22] Louis A 1986 Incomplete data problems in x-ray computerized tomography 1. Singular value decomposition of the limited-angle transform *Numer. Math.* **48** 251–62
[23] Madych W and Nelson S 1986 Reconstruction from restricted Radon transform data: resolution and ill-conditionedness *SIAM J. Math. Anal.* **17** 1447–53
[24] Faridani A, Ritman E L and Smith K T 1992 Local tomography *SIAM J. Appl. Math.* **52** 459–84
[25] Faridani A, Finch D V, Ritman E L and Smith K T 1997 Local tomography II *SIAM J. Appl. Math.* **57** 1095–127
[26] Katsevich A and Ramm A 1996 Pseudolocal tomography *SIAM J. Appl. Math.* **56** 167–91
[27] Rashid-Farrokhi F, Liu K J R, Berenstein C A and Walnut D 1997 Wavelet-based multiresolution local tomography info *IEEE Trans. Image Process.* **6** 1412–30
[28] Cormack A M 1964 Representation of a function by its line integrals with some radiological applications II *J. Appl. Phys.* **35** 2908–13
[29] Louis A 1981 Ghosts in tomography, the null space of the Radon transform *Math. Methods Appl. Sci.* **3** 1–10
[30] Royden H L 1968 *Real Analysis* 2nd edn (New York: Macmillan)
[31] DeStafano J and Olson T 1994 Wavelet localization of the Radon transform *IEEE Trans. Signal Process.* **42**